PCCP

Accepted Manuscript

ROYAL SOCIETY OF CHEMISTRY

www.rsc.org/pccp

Graphics for manuscript

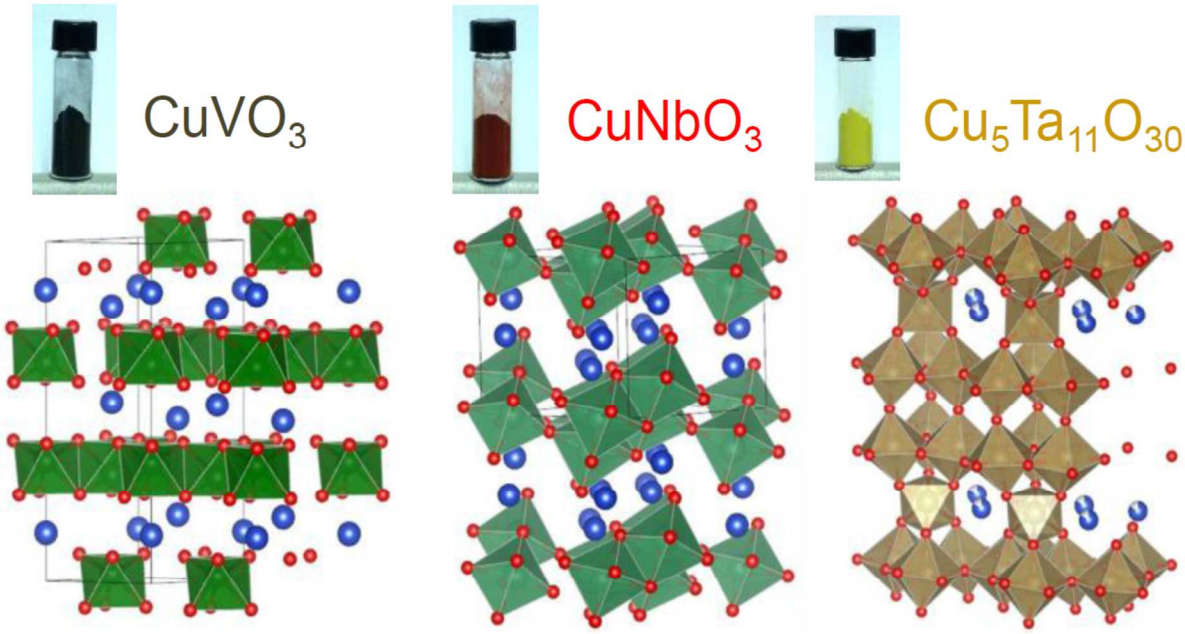

A joint theoretical and experimental investigation was conducted on the optoelectronic properties of $CuVO_3$, $CuNbO_3$ and $Cu_5Ta_{11}O_{30}$ materials.

Journal Name

RSCPublishing

ARTICLE

Screened coulomb hybrid DFT investigation on band gap and optical absorption predictions of $CuVO_3$, $CuNbO_3$ and $Cu_5Ta_{11}O_{30}$ materials

Cite this: DOI: 10.1039/x0xx00000x

Received 00th January 2012,
Accepted 00th January 2012

DOI: 10.1039/x0xx00000x

www.rsc.org/

Moussab Harb,* Dilshad Masih, and Kazuhiro Takanabe*

We present a joint theoretical and experimental investigation on the optoelectronic properties of $CuVO_3$, $CuNbO_3$ and $Cu_5Ta_{11}O_{30}$ materials for potential photocatalytic and solar cell applications. In addition to the experimental results obtained by powder X-ray diffraction and UV-Vis spectroscopy on the materials synthesized under flowing N_2 gas at atmospheric pressure via solid-state reactions, the electronic structure and UV-Vis optical absorption coefficient of these compounds are predicted with high accuracy using advanced first-principles quantum methods based on DFT (including the perturbation theory approach DFPT) within the screened coulomb hybrid HSE06 exchange-correlation formalism. The calculated density of states are found to be in agreement with the UV-Vis diffuse reflectance spectra, predicting a small indirect band gap of 1.4 eV for $CuVO_3$, a direct band gap of 2.6 eV for $CuNbO_3$, and an indirect (direct) band gap of 2.1 (2.6) eV for $Cu_5Ta_{11}O_{30}$. It is confirmed that the Cu(I)-based multi-metal oxides possess a strong contribution of filled Cu(I) states in valence band and of empty d^0 metal states in conduction band. Interestingly, $CuVO_3$ with its predicted small indirect band gap of 1.4 eV shows the highest absorption coefficient in the visible range with a broad absorption edge extending to 886 nm. This novel result offers a great opportunity to this material to be an excellent candidate for solar cell applications.

Introduction

The development of artificial photosynthesis is one of the greatest scientific challenges of our times, not only to protect the environment but also to ensure global economic security. To mimic the natural photosynthesis process, a complete understanding of the natural photosynthesis process at the molecular level is essential to enable the production of inexpensive, lightweight, and high-energy-density fuels. Artificial photosynthesis may involve photo/electrocatalytic H_2 generation by water splitting or the use of H_2 in combination with atmospheric/industrially sourced carbon dioxide (CO_2) conversion products to provide a continuous supply of high-energy carrier fuels at small/medium scales.[1,2] Recently, Cu_2O has received considerable attention in various energy-conversion applications, including photo/electrochemical hydrogen production[3-5] and the photo/electrochemical conversion of CO_2 to energy-carrier fuels.[6-9] The Cu(I) state, with its d^{10} electronic configuration, has been proposed to be active for various photo/electrochemical and catalytic reactions.[8-18] For electrochemical CO_2 reduction, Cu(I) sites are proposed to stabilize reaction intermediates such as CO, carbonates (CO_2^{3-}), formates ($HCOO^-$), and methoxy (H_3CO^-) adsorbates, as expected from their high heats of adsorption.[19,20] Although the Cu(I) state makes these materials attractive, the stability of Cu(I) species toward redox reactions remains an issue to be solved.

The intrinsic redox properties of materials are critical for these solar fuel production techniques. Under H_2 conditions, CuO can be sequentially reduced to Cu_2O and eventually to metallic Cu, as expected from the measured apparent activation energies for the reduction of CuO and Cu_2O of approximately 60.7 kJ mol^{-1} and 115 kJ mol^{-1}, respectively.[21] Metallic copper, however, can be sequentially thermally oxidized (Cu → Cu_2O → CuO), where an activation barrier needs to be overcome because of the crystallographic constraints.[21] The electrochemical standard reduction potentials for Cu(I) and (II) ions to metallic states are 0.520 and 0.340 V vs. SHE, respectively, which suggests that the Cu(I) should be more easily reduced than Cu(II) on the basis of thermodynamics. Notably, these reduction potentials are more positive than the standard reduction potentials of CO_2 reduction or hydrogen evolution. This makes the materials more difficult to be stabilized.

To overcome the instability of Cu(I) species in cuprous oxide, an alternative approach was proposed by mixing Cu(I) with a second metal (group 5) and increasing the Cu-O bond strength. This type of Cu(I) containing multi-metal oxides have been synthesized since the early 1970s for electronic, magnetic, optical, gas-sensing, catalysis, and lithium-ion batteries.[22-27] The authors of previous reports have stressed that phases of this composition can only be attained at high pressures in an evacuated sealed reactor,[22,28,29] which makes the synthesis process quite tedious. In recent years, Maggard and coworkers

have reported a solid-state synthesis of $CuNbO_3$ and $Cu_5Ta_{11}O_{30}$ semiconducting compounds in evacuated fused-silica tubes for photoelectrochemical applications.[30] The study was accompanied by density of states calculations using the linear muffin-tin orbital (LMTO) and the DFT-PBE methods. An indirect band gap of 0.85 eV was predicted for $Cu_5Ta_{11}O_{30}$ while a direct band gap of 2.0 eV was obtained for $CuNbO_3$. It is important to stress here that the two standard methods adopted by the authors are well-documented to provide a strong underestimation of the band gap of semiconductors. Recent hybrid DFT methods yield a much more improved description of these band gaps,[31-35] as highly required here for giving correct information about these materials. In addition, no accurate simulation of the UV-Vis optical absorption response was carried out for giving more relevant interpretation of the experimental results.

In this paper, we report a joint theoretical and experimental investigation on the optoelectronic properties of $CuVO_3$, $CuNbO_3$ and $Cu_5Ta_{11}O_{30}$ materials prepared in our laboratory using a solid-state synthesis at atmospheric pressure under an inert gas flow. Our present work brings rational insights into the electronic structure and UV-Vis optical absorption coefficient of these compounds using accurate first-principles quantum methods based on DFT (including the perturbation theory approach DFPT) within the screened coulomb hybrid HSE06 exchange-correlation formalism. We stress here that the novel properties for $CuVO_3$ predicted by our calculations offer a great opportunity to this material to be used in solar cell applications. To the best of our knowledge, no DFT study has been previously reported on this compound.

Results and discussion

Structural characterization

Powder XRD patterns of the products obtained from the reaction of oxide precursors for $CuVO_3$, $CuNbO_3$, and $Cu_5Ta_{11}O_{30}$ are presented in Figure 1. The XRD patterns for $CuVO_3$ indicated the crystallization of $CuVO_3$ (PDF 00-024-0378) or the $Cu_{6.78}V_6O_{18.78}$ phase (PDF 01-072-1727), which is commonly reported as the $CuVO_3$ phase at 773 K and beyond.[36,37] Three main characteristic XRD peaks of $CuVO_3$ appeared in the 2θ range of 30–35°. Powder XRD patterns of the product obtained at 823 K contained sharp and well-resolved X-ray diffraction peaks that indicated the formation of pure-phase $CuVO_3$; no characteristic peaks from the intermediate or the precursors were observed. $CuVO_3$ has an ilmenite-type lamellar structure, as shown in Figure 2.[38] All the same VO_6 octahedral units in the *ab* plane compose one sheet of the layered structure. The sheets are stacked along the *c* direction, with copper species sandwiched between them. No connections between VO_6 sheets are present along the *c* direction. The copper species are also octahedrally coordinated, and all are alike.

The powder XRD pattern in Figure 1 also reveals the crystalline nature of the $CuNbO_3$ product prepared from Cu_2O and Nb_2O_5. $CuNbO_3$ was crystallized within 1 h at 1173 K under a high flow of nitrogen. Previous studies on $CuNbO_3$ have reported long reaction times of up to 24 h for the crystallization in evacuated fused silica tubes.[26,28-30] However, even after long reaction times, the crystallinity of $CuNbO_3$ remained comparatively poor and coexisted with a secondary phase of $CuNb_3O_8$ impurity.[24,29,30,39-41] The structure of $CuNbO_3$ is ABO_3 lamellar-type, as shown in Figure 2. All the niobium species possess octahedral symmetry. $CuNbO_3$ exhibits a monoclinic crystal system with a *C*2/*m* space group.[24,28,42]

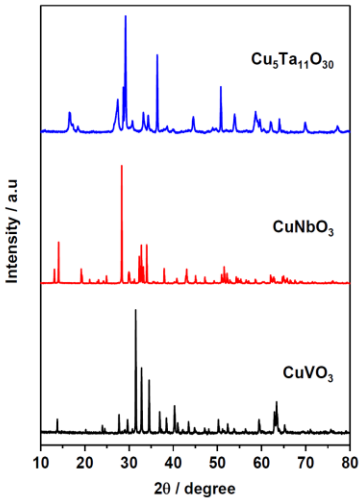

Figure 1. Powder XRD patterns of (a) $CuVO_3$, (b) $CuNbO_3$, and (c) $Cu_5Ta_{11}O_{30}$ synthesized through solid-state reactions.

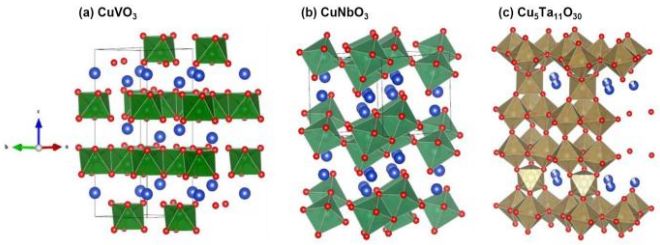

Figure 2. Polyhedral model structures of (a) $CuVO_3$; Cu (blue spheres), V (green spheres), and O (red spheres); (b) $CuNbO_3$; Cu (blue spheres), Nb (sea-green spheres), and O (red spheres); and (c) $Cu_5Ta_{11}O_{30}$; Cu (blue spheres), Ta (yellow-green spheres), and O (red spheres).

In contrast to the monomeric VO_6 species in $CuVO_3$, two types of NbO_6 octahedra exist in the $CuNbO_3$ structure. These two types of NbO_6 run parallel in the *ab* plane, making a zigzag-type sheet of double octahedral layers. Each layer of the NbO_6 octahedra is connected by corner-sharing within the layer. Both the NbO_6 layers in the *ab* plane are connected by edge-sharing with the neighboring unit. Octahedral NbO_6 sheets are stacked along the *c* direction, and two copper species are entangled between the sheets; these species have different lengths of Cu-O bonds with the surrounding ten oxygen atoms.

For Cu(I) tantalates, well-resolved, intense XRD peaks of the $Cu_5Ta_{11}O_{30}$ phase were observed in the XRD pattern of the product of the solid-state synthesis conducted at 1373 K, as shown in Figure 1. A scheme of the $Cu_5Ta_{11}O_{30}$ structure is shown in Figure 2.[43] Two distinct types of polyhedral TaO_x species, TaO_6 and TaO_7, are present in the structure of $Cu_5Ta_{11}O_{30}$. Along with two polyhedral TaO_x species, two distinct types of sheets are stacked alternately in the $Cu_5Ta_{11}O_{30}$ structure. In one of the sheets of the TaO_x, two layers of decahedral TaO_7 are spread across the *ab* plane. Within one sheet, both the decahedral TaO_7 layers in the *ab* plane are connected by corner-sharing. The other sheet is composed of only one layer of edge-sharing TaO_7 species. The sheet types were stacked alternately along the *c* direction. Copper species

are present between the decahedral TaO_7 sheets, in the surroundings of the octahedral TaO_6 species. In contrast to the exposed copper species in the *ab* planes of the vanadate and niobate structures, the copper species in the $Cu_5Ta_{11}O_{30}$ structure are completely surrounded by polyhedral TaO_x. Table S1 in supporting information reports the various M-O bond lengths obtained from DFT-optimized structures shown in Figure 2.

The phase transformation of the materials to stoichiometric compounds with respect to crystallization temperature is important and can be rationalized on the basis of the dissociation energy of the precursors. Solid-state synthesis follows a diffusion-limited process, utilizing the ionic mobility of the metal cations and the oxygen anions at high temperatures.[44] $CuVO_3$, $CuNbO_3$, and $Cu_5Ta_{11}O_{30}$ were crystallized at 823, 1173, and 1373 K, respectively. The synthesis results revealed an interesting trend of Cu(I) mixed oxides with increasing atomic weights and bond dissociation energies within group 5, consistent with the increase in the dissociation energies ($D°_{298}$) of the V-O, Nb-O, and Ta-O bonds, which are 637, 726.5 ± 10.6, and 839 kJ mol^{-1}, respectively.[45] Although $CuTaO_3$ has been reported to be prepared at high pressure (65 kbar), $CuTaO_3$ is not stable at atmospheric pressure because the Cu(I) ions of $CuTaO_3$ are oxidized to Cu(II) thus, $CuTa_2O_6$ is the pseudo-stable phase under such conditions. Nevertheless, the $CuNbO_3$ structure with distorted monoclinic symmetry and the $CuVO_3$ structure are stable even at atmospheric pressures, as confirmed by our XRD results (Figure 1).[46] The SEM images (Figure S1) and surface areas are described in the Supplementary Information.

UV-Vis optical absorption properties and electronic structure

Figure 3 shows the DR-UV-Vis spectra of the Cu(I)-group 5 metal oxides along with the spectrum of Cu_2O as a reference. The DR-UV-Vis spectrum for $CuVO_3$ exhibited an extended absorption throughout the visible and near-IR regions, consistent with the dark color of the product. No clear absorption edge was observed up to 1100 nm for the $CuVO_3$ synthesized at 823 K, probably because of non-stoichiometric structure giving metallic nature in the material. Optical spectra were also recorded to monitor the growth of crystalline $CuNbO_3$ under various solid-state reaction conditions. With the complete transformation of the precursors at 1173 K, one sharp absorption edge at approximately 580 nm was observed in the spectrum of the cherry-red-colored $CuNbO_3$. The allowed direct band gap of $CuNbO_3$ determined from the Tauc plot was approximately 2.1 eV, which is similar to the value reported by Maggard and co-workers (2.0 eV).[30,39] An elevated baseline was observed for $CuNbO_3$ beyond the absorption edge, which suggests the presence of Cu-deficient or reduced sites.[30] $CuNbO_3$ prepared in the presence of excess Cu_2O precursor resulted in a spectrum with a lower baseline intensity, and the product exhibited an enhanced XRD crystalline nature. The optical spectrum for the $Cu_5Ta_{11}O_{30}$ obtained from the solid-state reaction of stoichiometric ratios at 1373 K showed one clear absorption edge at approximately 460 nm. With respect to the highest temperature of crystallization, the lowest baseline intensity was observed for $Cu_5Ta_{11}O_{30}$ among all the Cu(I)-group 5 metal oxides obtained from the stoichiometric ratios of the precursors. In accordance with the literature, the allowed direct band gap of $Cu_5Ta_{11}O_{30}$ determined from the Tauc plot was approximately 2.7 eV. The latest studies have reported an experimental band gap of approximately 2.6 eV for $Cu_5Ta_{11}O_{30}$.[26,47]

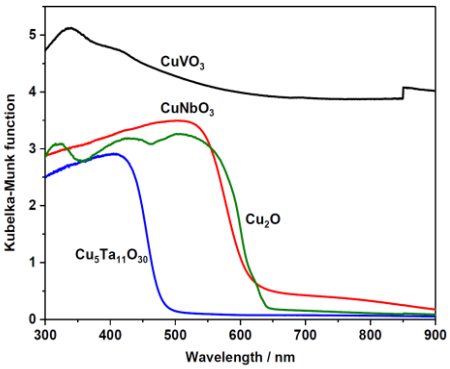

Figure 3. UV-Vis spectra of Cu_2O, $CuVO_3$, $CuNbO_3$, and $Cu_5Ta_{11}O_{30}$.

Figure 4 shows the calculated electronic density of states and energy dispersion curves of these materials with the DFT-HSE06 method. For $CuVO_3$, our electronic analysis revealed a valence bandwidth within 0-2.0 eV range below the Fermi level, which is mainly composed of fully occupied Cu 3d states, and a conduction band primarily consists of empty V 3d states (Figure 4a). Our HSE06 calculations predict this compound to be an indirect (Γ-M) semiconductor with small band gap energy of 1.4 eV, as shown in Figure 4a. The lowest-energy band gap in this material originates from indirect Cu $3d^{10}$-V $3d^0$ orbital transitions. To the best of our knowledge, no DFT study has been previously reported on this compound. Note that our HSE06 band gap value of 1.4 eV is predicted with high accuracy. However, the remarkable discrepancy with the current DR-UV-Vis data may arise from the important contributions of non-stoichiometric phases such as $Cu_{6.78}V_6O_{18.78}$ (as mentioned above) which might significantly affect the conductivity of the original $CuVO_3$ one. In the case of $CuNbO_3$, the valence band states located within 0-2.6 eV range below the Fermi level are dominated by fully filled Cu 3d states, whereas the conduction band states are mainly composed of unoccupied Nb 4d states (Figure 4b). This material is identified as a direct semiconductor with band gap energy of 2.6 eV (see Figure 4b) which is slightly larger than the measured one (2.1 eV; Figure 3). Here, the direct electronic excitations from Cu $3d^{10}$ orbitals to Nb $4d^0$ orbitals characterize the lowest-energy band gap. Our calculated direct band gap is found to show discrepancy of 0.5 eV compared to the current experimental data. Note that our predicted band gap value of 2.6 eV with HSE06 closely matches the experimental data obtained by Yamazoe et al.[27] In the case of $Cu_5Ta_{11}O_{30}$, the analysis shows a valence bandwidth within 0-2.6 eV range below the Fermi level, mainly occupied by electronic Cu 3d states, and a conduction band dominated by empty electronic Ta 5d states (Figure 4c). For this compound, an indirect (Γ-M) semiconductor with a band gap energy of 2.1 eV is predicted (Figure 4c), which was not observed experimentally (Figure 3). The calculated direct band gap energy at the M point is 2.6 eV (Figure 4c), which is closer to the experimental value in Figure 3. The lowest-energy band gap in this compound involves indirect transitions between the Cu $3d^{10}$ orbitals and the Ta $5d^0$ orbitals. Our calculated direct band gap with HSE06 closely matches the current experimental data as well as the previous data reported by Palasyuk et al.,[47] but we currently cannot explain lack of indirect counterpart in the experimental predicted by the calculation. In all cases, the contributions of O

2p orbitals to the valence band states located within 0-2.6 eV range below the Fermi levels were observed to be very weak. This strong localization of the valence band states on Cu 3d orbitals, as well as the lack of strong mixings with O 2p orbitals connecting the Cu planes, lead to a limited probability of hole mobility in these materials.[33]

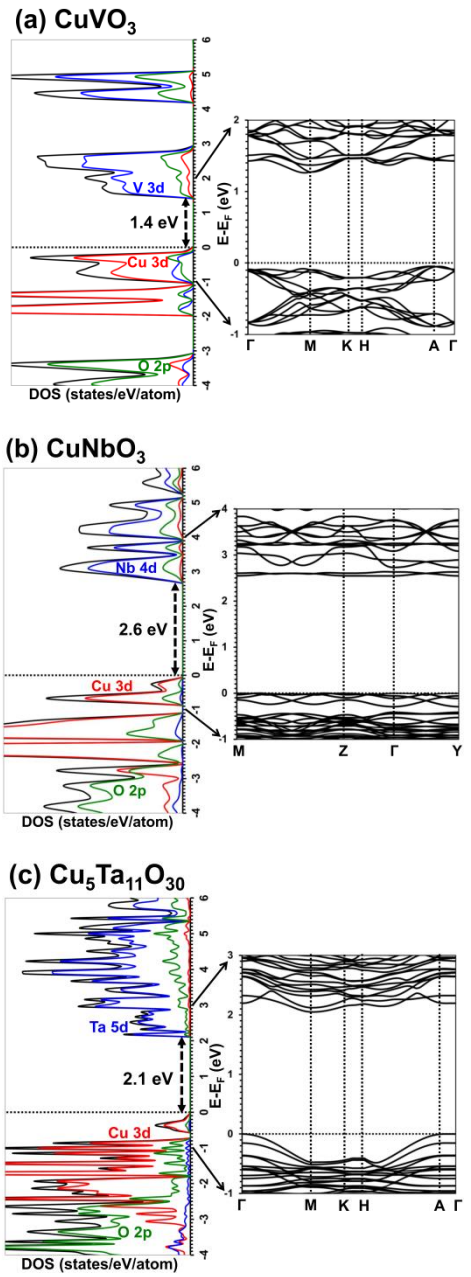

Figure 4. Electronic density of states and band structure k-space diagrams calculated with the DFT-HSE06 method for: (a) $CuVO_3$, (b) $CuNbO_3$, and (c) $Cu_5Ta_{11}O_{30}$. Color legend: total DOS (black) and the projected orbital contributions from Cu 3d orbitals (red), O 2p orbitals (green), and V 3d, Nb 4d, or Ta 5d orbitals (blue). The black dashed horizontal lines indicate the Fermi levels.

To determine the fraction of the light absorbed in these materials, we calculated their optical absorption coefficient as a function of the wavelength of incident light following the methodology described in the theoretical methods section. The calculated spectra of $CuVO_3$, $CuNbO_3$ and $Cu_5Ta_{11}O_{30}$ materials with the DFPT-HSE06 method are shown in Figure 5. The spectrum of $CuVO_3$ revealed the appearance of high-intensity resonant bands in the visible range, with a broad absorption edge extending to 886 nm (black curve). In the cases of $CuNbO_3$ and $Cu_5Ta_{11}O_{30}$, the spectra exhibit roughly similar behavior represented by low-intensity absorption features appearing in the visible range and broad edges extending to 477 and 590 nm, respectively (red and blue curves). Importantly, the optical density between 400 and 600 nm is found to be much higher in the case of $CuVO_3$ than in $CuNbO_3$ or $Cu_5Ta_{11}O_{30}$. The major difference here can be strongly correlated with the higher density of Cu 3d states located within 0.7 eV just below the Fermi level in $CuVO_3$ as compared with those located within 0.5 or 0.9 eV below the Fermi levels in the case of $CuNbO_3$ or $Cu_5Ta_{11}O_{30}$.

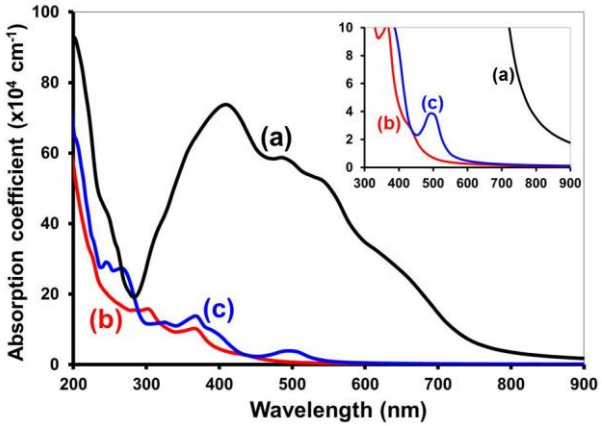

Figure 5. UV-Vis optical absorption coefficient spectra calculated with the DFPT-HSE06 method for: (a) $CuVO_3$, (b) $CuNbO_3$, and (c) $Cu_5Ta_{11}O_{30}$. The absorption edges are displayed in the inset figure.

In summary, the computational approach adopted in this study showed improved accuracy in the prediction of optical absorption properties originating from the precise calculation of the electronic structure. This methodology may be extended to the identification of good photocatalytic and solar cell materials among novel semiconductors, with a focus not only on the band gap but also on the hole and electron mobility. This robust and advanced methodology may be extended to the identification of novel semiconducting materials for a large variety of technological applications.

Conclusions

We have presented a joint theoretical and experimental investigation on the optoelectronic properties of $CuVO_3$, $CuNbO_3$ and $Cu_5Ta_{11}O_{30}$ materials. Our study brought rational insights into the electronic structure and UV-Vis optical absorption coefficient of these compounds using accurate first-principles quantum calculations based on DFT (including the perturbation theory approach DFPT) within the screened coulomb hybrid HSE06 exchange-correlation formalism. The calculated density of states showed good agreement with the UV-Vis diffuse reflectance spectra, predicting a small indirect band gap of 1.4 eV for $CuVO_3$, a direct band gap of 2.6 eV for $CuNbO_3$, and an indirect (direct) band gap of 2.1 (2.6) eV for $Cu_5Ta_{11}O_{30}$. We confirmed that the Cu(I)-based multi-metal

oxides possess a strong contribution of filled Cu(I) states in valence band and of empty d^0 metal states in conduction band. Interestingly, $CuVO_3$ with its predicted small indirect band gap of 1.4 eV showed the highest absorption coefficient in the visible range with a broad absorption edge extending to 886 nm. This novel result will certainly offer a great opportunity to this material as a good candidate for, e.g., solar cell applications.

Experimental and Theoretical Methods

Synthesis of $CuVO_3$, $CuNbO_3$, and $Cu_5Ta_{11}O_{30}$

Cu_2O (Aldrich; minimum 99%) and group 5 metal oxides (V_2O_5, Nb_2O_5, Ta_2O_5; all Aldrich, 99.9%) were used as precursors for the synthesis of $CuVO_3$, $CuNbO_3$, and $Cu_5Ta_{11}O_{30}$, respectively. Precursor powders with stoichiometric ratios were thoroughly homogenized in an agate mortar with a pestle. The obtained mixture was placed in an alumina boat and treated in a tube furnace (Nabertherm RS 80/300/13, tube I.D. 70 mm) under a high flow of nitrogen gas (1.5 L min^{-1}). The temperature was increased at a rate of 5 K min^{-1} to the required crystallization temperature and was maintained at that temperature for up to 5 h. Both ends of the tube furnace were enclosed in a jacket of cooling water, and the furnace exhibited good temperature stability at the programmed value. After a specific reaction time, the furnace was allowed to cool under flowing nitrogen, and the products were removed when the temperature was normalized to room temperature. Each reaction product was ground to a fine powder and subsequently characterized using various techniques.

Characterization

Powder X-ray diffraction (XRD) patterns in the 2θ range 10–80° were recorded to investigate the crystalline nature and phase purity of the products. XRD patterns of the powder samples were recorded on a Bruker model D8 Advance. Cu Kα radiation from a Cu anode X-ray tube operated at 40 kV and 40 mA was used as an X-ray source for collecting the XRD patterns. Optical properties of the obtained powder samples were studied by diffuse reflectance ultraviolet-visible (DR-UV-Vis) spectrophotometry on a JASCO model V-670 spectrophotometer equipped with an integrating sphere. The spectra were scanned from the UV to the near-IR region under irradiation by a deuterium lamp and a halogen lamp; the data were processed using the Kubelka-Munk function.

Theoretical methods

For electronic density of states (DOS) and k-space band-structure calculations of $CuVO_3$, $CuNbO_3$, and $Cu_5Ta_{11}O_{30}$ materials, we employed DFT within the HSE06[48,49] exchange-correlation formalism using VASP5.2 program.[50-52] The crystal structures of these materials were fully optimized at the DFT-PBE level. The valence atomic configurations adopted in the calculations were $3d^{10}4s^1$ for Cu, $3p^6 3d^4 4s^1$ for V, $4p^6 4d^4 5s^1$ for Nb, $5d^3 6s^2$ for Ta, and $2s^2 2p^4$ for O. The Brillouin zones of $CuVO_3$, $CuNbO_3$, and $Cu_5Ta_{11}O_{30}$ were sampled with 6 × 6 × 3, 4 × 4 × 4, and 5 × 5 × 2 Monkhorst-Pack *k*-point grids,[53] respectively. The tetrahedron method with Bloch corrections for the Brillouin zone integration was used for the DOS, whereas Gaussian smearing was adopted for the energy dispersion curves. As was recently reported in our theoretical studies on reference systems,[31-35] the use of the DFT-HSE06 approach leads to an accurate prediction of the experimental band gap of semiconducting materials.

For UV-Vis optical absorption calculations of these materials, we applied the density functional perturbation theory (DFPT), as implemented in VASP5.2[49-52] within the HSE06 formalism. The optical properties were determined through the frequency-dependent complex dielectric function $\varepsilon(\omega) = \varepsilon_1(\omega) + i\varepsilon_2(\omega)$ following a methodology described in the literature.[54] The real part $\varepsilon_1(\omega)$ was given by the Kramers-Kronig relation.[55,56] The imaginary part $\varepsilon_2(\omega)$ was calculated by summing all the possible transitions from occupied to unoccupied states in the Brillouin zone weighted with the matrix element describing the probability of transition. To determine the fraction of the light absorbed in these materials, we calculated the optical absorption coefficient (in cm^{-1}) of each compound as a function of the wavelength of incident light using the equation $\alpha(\omega) = \frac{4\pi}{\lambda} k(\omega)$, where λ and ω are the wavelength and frequency of the incident light, respectively, and $k(\omega)$ represents the extinction coefficient given by $k(\omega) = \left(\frac{\sqrt{\varepsilon_1^2 + \varepsilon_2^2} - \varepsilon_1}{2} \right)^{\frac{1}{2}}$. As a result of the accurate band gap determination provided by the DFT-HSE06 method, the use of the DFPT-HSE06 approach is expected to accurately describe the optical transitions in the UV-Vis range, as recently demonstrated in our theoretical studies on reference systems.[48-53]

Acknowledgements

The research reported in this publication was supported by the King Abdullah University of Science and Technology and by KAUST core labs.

Notes and references

[a] Division of Physical Sciences and Engineering, KAUST Catalysis Center (KCC), King Abdullah University of Science and Technology (KAUST), 4700 KAUST, Thuwal, 23955-6900, Kingdom of Saudi Arabia, E-mail: moussab.harb@kaust.edu.sa, kazuhiro.takanabe@kaust.edu.sa

† Electronic Supplementary Information (ESI) available: [Supplemental data for Cu(I)-based materials of SEM images and surface area]. See DOI: 10.1039/b000000x/

1 T. A. Faunce, W. Lubitz, A. W. Rutherford, D. MacFarlane, G. F. Moore, P. Yang, D. G. Nocera, T. A. Moore, D. H. Gregory, S. Fukuzumi, K. B. Yoon, F. A. Armstrong, M. R. Wasielewski and S. Styring, *Energy Environ. Sci.*, 2013, **6**, 695-698.

2 D. K. Bora, A. Braun and E. C. Constable, *Energy Environ. Sci.*, 2013, **6**, 407-425.

3 M. Hara, T. Kondo, M. Komoda, S. Ikeda, J. N. Kondo, K. Domen, M. Hara, K. Shinohara and A. Tanaka, *Chem. Commun.*, 1998, 357-358.

4 A. Paracchino, V. Laporte, K. Sivula, M. Grätzel and E. Thimsen, *Nat Mater*, 2011, **10**, 456-461.

5 C. Li, Y. Li and J.-J. Delaunay, *ACS Appl. Mater. Interfaces*, 2013.

6 C. W. Li and M. W. Kanan, *J. Am. Chem. Soc.*, 2012, **134**, 7231-7234.
7 M. Le, M. Ren, Z. Zhang, P. T. Sprunger, R. L. Kurtz and J. C. Flake, *J. Electrochem. Soc.*, 2011, **158**, E45-E49.
8 K. W. Frese, *J. Electrochem. Soc.*, 1991, **138**, 3338-3344.
9 A. T. Garcia-Esparza, K. Limkrailassiri, L. Frederic, S. Rasul, W. Yu, L. Lin and K. Takanabe, *J. Mater. Chem. A*, 2014, **2**, 7389-7401.
10 I. H. Tseng, W.-C. Chang and J. C. S. Wu, *Appl. Catal. B Environ*, 2002, **37**, 37-48.
11 J. C. S. Wu, H.-M. Lin and C.-L. Lai, *Appl. Catal. A: general*, 2005, **296**, 194-200.
12 O.-S. Joo, K.-D. Jung, I. Moon, A. Y. Rozovskii, G. I. Lin, S.-H. Han and S.-J. Uhm, *Ind. Eng. Chem. Res.*, 1999, **38**, 1808-1812.
13 X.-M. Liu, G. Q. Lu, Z.-F. Yan and J. Beltramini, *Ind. Eng. Chem. Res.*, 2003, **42**, 6518-6530.
14 G. C. Chinchen, M. S. Spencer, K. C. Waugh and D. A. Whan, *Journal of the Chemical Society, J. Chem. Soc., Faraday Trans. 1: Phys. Chem. Condens. Phases*, 1987, **83**, 2193-2212.
15 G. C. Chinchen, K. C. Waugh and D. A. Whan, *Appl. Catal*, 1986, **25**, 101-107.
16 M. Saito and K. Murata, *Catal Surv Asia*, 2004, **8**, 285-294.
17 J. Wu, M. Saito, M. Takeuchi and T. Watanabe, *Appl. Catal. A: general*, 2001, **218**, 235-240.
18 H. Nakatsuji and Z.-M. Hu, *Int. J. Quantum Chem*, 2000, **77**, 341-349.
19 S. Bailey, G. F. Froment, J. W. Snoeck and K. C. Waugh, *Catal. Lett.*, 1994, **30**, 99-111.
20 R. G. Herman, K. Klier, G. W. Simmons, B. P. Finn, J. B. Bulko and T. P. Kobylinski, *J. Catal.*, 1979, **56**, 407-429.
21 J. Y. Kim, J. A. Rodriguez, J. C. Hanson, A. I. Frenkel and P. L. Lee, *J. Am. Chem. Soc.*, 2003, **125**, 10684-10692.
22 B. L. Chamberland, *J. Solid State Chem.*, 1970, **1**, 138-142.
23 Y. Inoue, *Energy Environ. Sci.*, 2009, **2**, 364-386.
24 V. Pralong, M. A. Reddy, V. Caignaert, S. Malo, O. I. Lebedev, U. V. Varadaraju and B. Raveau, *Chem. Mater.*, 2011, **23**, 1915-1922.
25 U. A. Joshi and P. A. Maggard, *J. Phys. Chem. Lett*, 2012, **3**, 1577-1581.
26 L. Fuoco, U. A. Joshi and P. A. Maggard, *J. Phys. Chem. C*, 2012, **116**, 10490-10497.
27 S. Yamazoe, S. Yanagimoto and T. Wada, *physica status solidi (RRL) – Rapid Research Letters*, 2011, **5**, 153-155.
28 A. W. Sleight and C. T. Prewitt, *Mater. Res. Bull.*, 1970, **5**, 207-211.
29 E. Wahlström and B.-O. Marinder, *Inorg. Nuc. Chem. Lett*, 1977, **13**, 559-564.
30 U. A. Joshi, A. Palasyuk, D. Arney and P. A. Maggard, *J. Phys. Chem. Lett*, 2010, **1**, 2719-2726.
31 M. Harb, *J. Phys. Chem. C*, 2013, **117**, 25229-25235.
32 M. Harb, *J. Phys. Chem. C*, 2013, **117**, 12942-12948.
33 M. Harb, D. Masih, S. Ould-Chikh, P. Sautet, J.-M. Basset and K. Takanabe, *J. Phys. Chem. C*, 2013, **117**, 17477-17484.
34 M. Harb, P. Sautet and P. Raybaud, *J. Phys. Chem. C*, 2013, **117**, 8892-8902.
35 M. Harb, P. Sautet and P. Raybaud, *J. Phys. Chem. C*, 2011, **115**, 19394-19404.
36 M. Kamiya, M. Eguchi, T. Miura and T. Kishi, *Solid State Ionics*, 1998, **109**, 321-326.
37 M. Nakamura, H. Namatame, A. Fujimori, A. Misu, S. Okatake, M. Onoda and H. Nagasawa, *J. Solid State Chem.*, 1994, **112**, 100-105.
38 J. R. Rea, P. W. Bless and E. Kostiner, *J. Solid State Chem.*, 1972, **5**, 446-451.
39 U. A. Joshi, A. M. Palasyuk and P. A. Maggard, *J. Phys. Chem. C*, 2011, **115**, 13534-13539.
40 P. E. W. B.O. Marinder, E. Wahlstrom, G. Malmros, *Acta Chem. Scand*, 1980, **34a**, 51-56.
41 J. M. Longo and A. W. Sleight, *Mater. Res. Bull.*, 1975, **10**, 1273-1277.
42 E. W. B.O. Marinder, *Chem. Scr.*, 1984, **23**, 157–160.
43 L. Jahnberg, *J. Solid State Chem.*, 1982, **41**, 286-292.
44 K. Takanabe and K. Domen, *ChemCatChem*, 2012, **4**, 1485-1497.
45 *CRC Handbook of Chemistry and Physics, 89th Edition*, 2009.
46 J. B. Goodenough and J. A. kafalas, *J. Solid State Chem.*, 1973, **6**, 493-501.
47 O. Palasyuk, A. Palasyuk and P. A. Maggard, *J. Solid State Chem.*, 2010, **183**, 814-822.
48 J. Heyd, G. E. Scuseria and M. Ernzerhof, *J. Chem. Phys.*, 2003, **118**, 8207-8215.
49 T. M. Henderson, J. Paier and G. E. Scuseria, *Phys. Status Solidi B*, 2011, **248**, 767-774.
50 G. Kresse and J. Furthmüller, *Phys. Rev. B*, 1996, **54**, 11169-11186.
51 G. Kresse and J. Hafner, *Phys. Rev. B*, 1994, **49**, 14251-14269.
52 G. Kresse and D. Joubert, *Phys. Rev. B*, 1999, **59**, 1758-1775.
53 H. J. Monkhorst and J. D. Pack, *Phys. Rev. B*, 1976, **13**, 5188-5192.
54 M. Gajdoš, K. Hummer, G. Kresse, J. Furthmüller and F. Bechstedt, *Phys. Rev. B*, 2006, **73**, 045112.
55 M. Launay, F. Boucher and P. Moreau, *Phys. Rev. B*, 2004, **69**, 035101.
56 S. Saha, T. P. Sinha and A. Mookerjee, *Phys. Rev. B*, 2000, **62**, 8828-8834.

